Experimental Analysis of the Stability of Retained Austenite in a Low-Alloy 42CrSi Steel after Different Quenching and Partitioning Heat Treatments

Alexander Liehr,* Thomas Wegener, Sebastian Degener, Artjom Bolender, Nico Möller, and Thomas Niendorf

Quenching and partitioning (Q&P) steels are characterized by an excellent combination of strength and ductility, opening up great potentials for advanced lightweight components. The Q&P treatment results in microstructures with a martensitic matrix being responsible for increased strength whereas interstitially enriched metastable retained austenite (RA) contributes to excellent ductility. Herein, a comprehensive experimental characterization of microstructure evolution and austenite stability is carried out on a 42CrSi steel being subjected to different Q&P treatments. The microstructure of both conditions is characterized by scanning electron microscopy as well as X-ray diffraction (XRD) phase analysis. Besides macroscopic standard tensile tests, RA evolution under tensile loading is investigated by in situ XRD using synchrotron and laboratory methods. As a result of different quenching temperatures, the two conditions considered are characterized by different RA contents and morphologies, resulting in different strain hardening behaviors as well as strength and ductility values under tensile loading. In situ synchrotron measurements show differences in the transformation kinetics being rationalized by the different morphologies of the RA. Eventually, the evolution of the phase specific stresses can be explained by the well-known Masing model.

1. Introduction

Overcoming the "high strength-high ductility trade-off", that is, limited formability with an increase in strength (and vice versa),

A. Liehr, T. Wegener, S. Degener, A. Bolender, N. Möller, T. Niendorf
Institute of Materials Engineering-Metallic Materials
University of Kassel
Mönchebergstraße 3, 34125 Kassel, Germany
E-mail: liehr@uni-kassel.de

S. Degener
Bundesanstalt für Materialforschung und -prüfung
Unter den Eichen 87, 12205 Berlin, Germany

(iD) The ORCID identification number(s) for the author(s) of this article can be found under https://doi.org/10.1002/adem.202300380.

has always been in focus of research activities in the field of materials science.[1,2] The ongoing demands for increasing resource efficiency and cost reduction, where the latter can be achieved by weight savings or inexpensive materials, play a decisive role here.[3] Specific sectors, such as the automotive industry, are highly interested in materials that can be used economically, while they offer highest performance, for example, a high level of crash safety, concomitantly. The urge for economic efficiency eventually promotes steady progress in lightweight construction, since weight reduction can save resources.[4] Especially in times of sustainable development, this goal gains in importance. In order to pave the way for substitutable materials, these must mechanically meet at least the same requirements as their established counterparts. As a consequence, highly stressed and safety-relevant components must guarantee at least the same or ideally even increased safety, while using less material and thus saving weight.[5] Safety can be considered as risk coverage, provided by the material resistance to incipient mechanical stress and protection against premature failure. Based on these requirements, the advanced high-strength steels (AHSS) were developed, whose attributes are characterized by cost reduction, weight and resource savings, as well as higher mechanical performance and reliability under both static and cyclic stresses.[6,7] The first generation of AHSS, whose representatives include dual-phase (DP) steels and transformation-induced plasticity (TRIP) steels, and the second generation with the well-known twinning-induced plasticity (TWIP) steels, are already well studied and used in application.[8,9] However, they offer potential for improvement in terms of achieving an optimal balance between strength and ductility while minimizing costs at the same time.[10] To further achieve this goal, Speer et al.[11] first introduced the process of quenching and partitioning (Q&P) in 2003, which established a potential basis for the third generation of AHSS. Eventually, this novel process allows to tailor a steel finally being characterized by the presence of elementary deformation mechanisms already well known, that is, the TRIP effect. However, its overall properties in terms of strength and ductility are further improved through a suitable heat treatment process.

The Q&P treatment aims to create a microstructure, in which tempered α′-martensite forms the matrix for interstitially enriched metastable retained austenite (RA).[12] Thereby, a distinction is often made between primary and secondary martensite.[13] The increased strength of the Q&P steels is, thus, due to the martensite matrix, while the (metastable) austenite contributes to excellent ductility and formability. The strain-induced martensitic phase transformation being characteristic for the TRIP effect (from γ-austenite to ε- and/or α′-martensite)[12,14] further improves the mechanical properties due to significant hardening. As a result of these outstanding mechanical properties, Q&P steels have been in focus of several studies pointing out the promising advantages of this new material class.[15] However, the majority of these studies only reported on microstructural characterization as well as mechanical properties focusing on monotonic strength and ductility. In ref. [16] the correlation between the austenite grain size and the differences in the mechanical behavior was investigated, based on different heat treatment strategies. Further studies also focused on the grain size as an influencing factor. However, differing conclusions are presented concerning this topic. While Wang et al.[17] reported that smaller austenite grains (i.e., 0.3–4 μm^2) are characterized by lower stability against strain-induced phase transformation, an increased mechanical stability (i.e., the resistance to phase transformation) is characteristic for smaller austenite grains according to Min et al.[18] They concluded that the carbon concentration is relatively high in small grains due to the overall smaller grain volume. In addition to the factors already mentioned affecting the mechanical stability of the RA, the strength of the phase surrounding the austenite is of significant importance.[19] The higher the strength of the matrix, the higher the mechanical stability of the austenite against the strain-induced phase transformation. This is supported by Jacques et al.[20] referring to this phenomenon as the so-called shielding effect. In other studies Fultz et al.[21,22] proposed that the dislocation density in the martensitic phase surrounding the austenite determines the degree to which the martensite is able to deform plastically to allow for the volume expansion that occurs during γ → α′ transformation. In addition to the dislocation density, the carbon content of the martensite also plays a decisive role as it affects the strength of the martensite and, thus, the capacity to accommodate the volume expansion of austenite upon transformation.[19] Furthermore, a hydrostatic pressure, which arises due to the formation of the martensitic phase during the Q&P treatment, is influential on the mechanical stability of the austenitic microstructure. Since the formation of a martensitic structure, as already mentioned, entails an expansion in volume, residual stresses arise as long as deformation cannot sufficiently be accommodated in the entire surrounding microstructure. A high hydrostatic pressure suppresses the strain-induced phase transformation and, thus, leads to increased mechanical austenite stability.[19] Hidalgo et al.[19] further concluded that a recovery of the martensite during tempering causes a reduction in residual stresses. This is accompanied by rearrangements and annihilation of dislocations, eventually leading to a reduction in the coherence between the austenite and martensite phases. This indeed favors martensitic nucleation and, thus, reduces austenite stability. In contrast, Fultz et al.[21] reported that the loss of coherence by tempering is minimal and that the dislocation structure

around the austenite is decisive for the nucleation of the martensite. A lower dislocation density in the martensitic microstructure reduces the stability of the austenite, since less energy is required to plastically deform the martensite during volume expansion in the γ → α′ transformation. Several studies investigating the mechanical behavior of Q&P steels were published by the group of Finfrock et al.[23,24] In their first study,[23] the authors showed that elevated strain hardening rates were achieved by the TRIP effect at high degrees of plastic strain. In addition, it was reported that neither the RA amount being present prior to straining nor the total RA amount transformed during straining were directly correlated to the mechanical performance under tensile load. Recently, Finfrock et al.[24] investigated the martensitic transformation in Q&P steels containing different RA amounts at dynamic strain rates using in situ synchrotron X-ray diffraction (XRD). A lower yield strength (YS) and a higher ductility were revealed for the condition containing a higher fraction of soft ferrite. Furthermore, the authors showed that prior to necking of the specimens the austenite content in both steels appeared to decrease in a similar fashion. In ref. [25], XRD measurements were likewise used to investigate the mechanical stability of RA during plastic compressive deformation of high-strength carbide-free bainitic steels.

As the introduction clearly outlines, many reports detailing on microstructure evolution in Q&P steels are already available in literature. However, a coherent understanding of the process–microstructure-property relationships in Q&P steels is still missing as some contradictory conclusions have been reported. This especially holds true with respect to the RA stability. However, first results presented in literature[24] show that in situ characterization by XRD experiments might pave the way for a more fundamental understanding of the martensitic transformation in Q&P steels. Thus, the motivation of the present study is to provide a thorough experimental characterization of microstructure evolution and austenite stability, respectively, of a Q&P steel subjected to external load. A low-alloyed 42CrSi was processed by two different Q&P heat treatments in order to obtain conditions with differing initial volume fractions of RA. Microstructural analysis was carried out by electron backscatter diffraction (EBSD). In addition to standard tensile tests, analysis of the RA was carried out by in situ XRD using synchrotron experiments in order to gain in-depth insights into the transformation behavior. Finally, the results obtained by the in situ synchrotron experiments are used to qualify less-expensive laboratory XRD methods. Here, a promising correlation of results is revealed.

2. Experimental Section

2.1. Low-Alloy 42CrSi Steel

The material in focus was the low-alloy 42CrSi steel with the chemical composition (determined by optical emission

Table 1. Chemical composition of the low-alloy 42CrSi steel obtained by optical emission spectroscopy (wt%).

C	Si	Mn	P	S	Cr	Mo	Ni	Al	Fe	Cu	Nb
0.40	1.96	0.67	0.015	0.014	3.16	0.041	0.096	0.022	93.4	0.14	0.029

spectroscopy) given in **Table 1**. Martensite start (M_S) and martensite finish (M_F) temperatures as well as the A_{c3} temperature of the material can be found in literature.[26–29] These temperatures were about 300, 180, and 845 °C, respectively. The 42CrSi steel represents a modification of materials widely used in the automotive sector, in particular for the production of transport vehicle components. Directly compared to similar materials, the 42SiCr steel contains a high silicon content eventually improving strength and fatigue resistance. Moreover, silicon hampers the formation of carbides and promotes diffusion of carbon into the austenite.[30–32] As shown in previous studies,[16,30] the RA in the alloy in focus can be adjusted very well by suitable heat treatments, which is why it is ideally suited for the investigations in the present work.

The material was provided as hot-rolled blank with a thickness of 11 mm. Different specimen geometries were used for the investigations conducted. As a first step, cuboid specimens with dimensions of 11 mm × 121 mm × 11 mm were obtained by water jet cutting with the longitudinal axis of all specimens being parallel to the rolling direction of the sheet. The final specimen geometries used are shown in **Figure 1**. For analysis of the microstructure and properties under monotonic tensile load, cylindrical specimens were machined by turning according to the geometry displayed in Figure 1a. Subsequent to

machining, the cylindrical specimens were subjected to two different Q&P heat treatments in order to obtain two conditions with differing RA contents. A general schematic detailing the Q&P process can be found in the work of Härtel et al.[16] The process routes employed in present work, referred to as QP170 and QP220 in the remainder of the article, are shown in Figure 1c. The two different routes considered were the results of a preliminary heat treatment study, which will not be discussed further for the sake of brevity. The steps of the two Q&P heat treatments are additionally listed in detail in **Table 2**. For further in-depth analysis of the austenite stability by in situ investigations, dog-bone-shaped specimens with a nominal gauge section of 18 mm × 1.5 mm × 1.6 mm (displayed in Figure 1b) were cut from the heat-treated cuboids by electro discharge machining (EDM). The loading direction (LD) of the specimens likewise was parallel to the rolling direction of the initial sheet.

Austenitizing without use of inert gases for both conditions was conducted at 950 °C for 70 min followed by air cooling in order to completely dissolve the carbon atoms in the face-centered-cubic (fcc) austenite lattice. The austenitizing was followed by a 2 min quenching step in a salt bath. The temperature of the salt bath was different for the two conditions in focus, that is, 220 °C for QP220 and 170 °C for QP170, respectively. Due to rapid
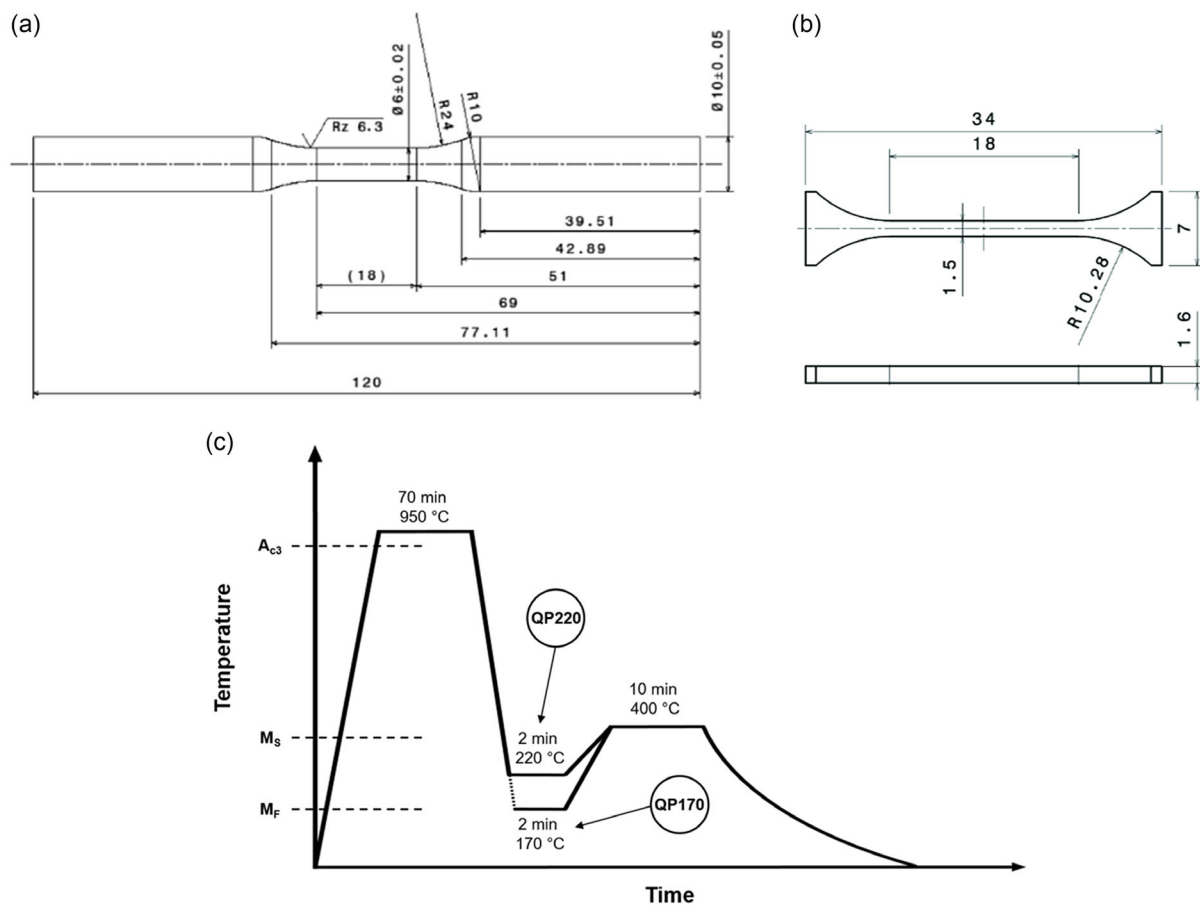

Figure 1. a) Geometry of the cylindrical specimen used for analysis of microstructure and properties under monotonic tensile load, b) dog-bone shaped specimen used for in situ analysis and c) temperature profiles for the heat treatments considered in present work.

Table 2. Q&P heat treatment routes applied for the two conditions QP220 and QP170, respectively.

Heat treatment step	Temperature [°C]	Time [min]	Medium	Condition
Austenitizing	950	70	Air	QP220
Quenching	220	2	Salt	
Partitioning	400	10	Sand	
Cooling	20	–	Air	
Austenitizing	950	70	Air	QP170
Quenching	170	2	Salt	
Partitioning	400	10	Sand	
Cooling	20	–	Air	

cooling, the martensitic transformation was promoted when reaching M_S. However, when cooling stopped at a temperature above M_F, the microstructure at this point was composed of martensite and austenite. Thereby, higher quenching temperatures in this step of the heat treatment resulted in an increased austenite content. The last step of the Q&P heat treatment was the partitioning. This step comprised 10 min at 400 °C (in hot sand) followed by air cooling. During partitioning the austenite was stabilized due to the diffusion of carbon from the supersaturated martensite into the austenite. It has to be noted that the temperatures during heat treatment were only controlled by the heating devices used. Thus, the exact specimen temperatures were not logged by a thermocouple. As a result, exact temperature profiles of the specimen including heating or cooling rates were not provided at this point.

2.2. Microstructural Characterization and Mechanical Testing

Microstructure analysis was carried out using a Zeiss ULTRA GEMINI high-resolution scanning electron microscope (SEM) operated at 20 kV. The SEM system was equipped with an EBSD unit. For EBSD characterization, cross sections of the cylindrical specimens were mechanically ground down to 5 μm grit size using SiC paper and further polished using a diamond suspension to a minimum of 1 μm. As a final step of preparation, vibration polishing was carried out for 16 h using conventional oxide polishing suspension (OPS) with a grain size of 0.25 μm. The measurements were performed at a working distance, magnification, and step size of 12 mm, 1000×, and 0.075 μm, respectively. Bruker Esprit software was used for data postprocessing, that is, removal of wild spikes and nonindexed points, taking at least five neighbor points into account. Monotonic tensile tests on the as-turned cylindrical specimens (see Figure 1a) were carried out using a digitally controlled servohydraulic test rig equipped with a 63kN load cell. The uniaxial tensile tests were performed under displacement control with a constant crosshead speed of 2 mm min^{-1}. For strain measurement, a Sandner extensometer featuring a maximum strain capability of 50% was used. Every tensile test was carried out until final failure of the specimen. In total, three tensile tests were performed for each condition considered.

2.3. Assessment of the RA Evolution Based on In Situ XRD Experiments

In the following, the concepts used for assessment of the RA are presented for the preliminary investigations as well as the in situ experiments under synchrotron (transmission mode) and laboratory (reflection mode) conditions. It has to be noted that due to the different measuring modes, the calculated stress components were different: While in transmission mode the main stress components in LD were determined by $\sigma_{11} - \sigma_{22}$ and by $\sigma_{33} - \sigma_{22}$, the well-known $\sin^2\psi$ approach was used to calculate the stress components based on $\sigma_{11} - \sigma_{33}$ and $\sigma_{22} - \sigma_{33}$ in reflection mode. For a more detailed explanation of determination of the stress components, the reader is referred to another study.[33] In both in situ studies, a miniature stress rig (Kammrath & Weiss, see **Figure 2**b) with a maximum load capability of 10 kN was used. The specimens were clamped in the stress rig and initially probed in a load-free state. After initially applying a preforce of about 100 N to set the clamping tools, the actual experiments were conducted. In contrast to the tensile tests conducted on the cylindrical specimens, where strains were measured by an extensometer, stress–strain diagrams obtained using the miniature stress rig were plotted taking into account strains calculated by evaluating the displacement data and the nominal specimen gauge length of 18 mm (see Figure 1b). Both the synchrotron and the XRD laboratory investigations were carried out using ground specimens. Specimens were mechanically ground to 5 μm grit size using SiC paper. At this point it has to be noted that the authors were aware of the complex microstructure of the steel considered, eventually consisting of austenite, martensite as well as fractions of ferrite and potentially also bainite. However, martensite, bainite, and ferrite were not specifically assessed in present work due to the fact that the XRD reflections of these phases were hard to separate, all being represented by the body-centered-cubic (bcc) crystal structure. Focus in present work was mainly on the evolution of the austenite upon loading. The experimental approach followed in the present work was previously proposed for a high-energy synchrotron diffraction study of a high-strength TRIP steel during tensile deformation by Kromm et al.[34] For RA evaluation in both in situ experiments considered here, the well-known phase specific proportional factors of the integral intensity (R-values)[35,36] were needed. In contrast to tables for determination of the R-values for laboratory experiments given in literature, R-values for the specific wavelength in the synchrotron experiments were not available and, thus, had to be calculated or evaluated, respectively. Further details will be given in Section 2.3.1. In addition, for both in situ experiments detailed in the following, diffraction elastic constants (DEC) given in **Table 3** were used to evaluate the stresses based on the measured strains.

2.3.1. Synchrotron Experiments

The time resolved in situ measurements were performed in a transmission mode setup at the PETRA III beamline P02.1 at DESY in Hamburg.[37] For this experiment an X-ray energy of 59.718 keV, an exposure time of 1 s, and a beam size of 1×1 mm^2 were used. To detect the full Debye–Scherrer rings (DSRs), a Perkin Elmer XRD 1621 area detector (with 2048×2048
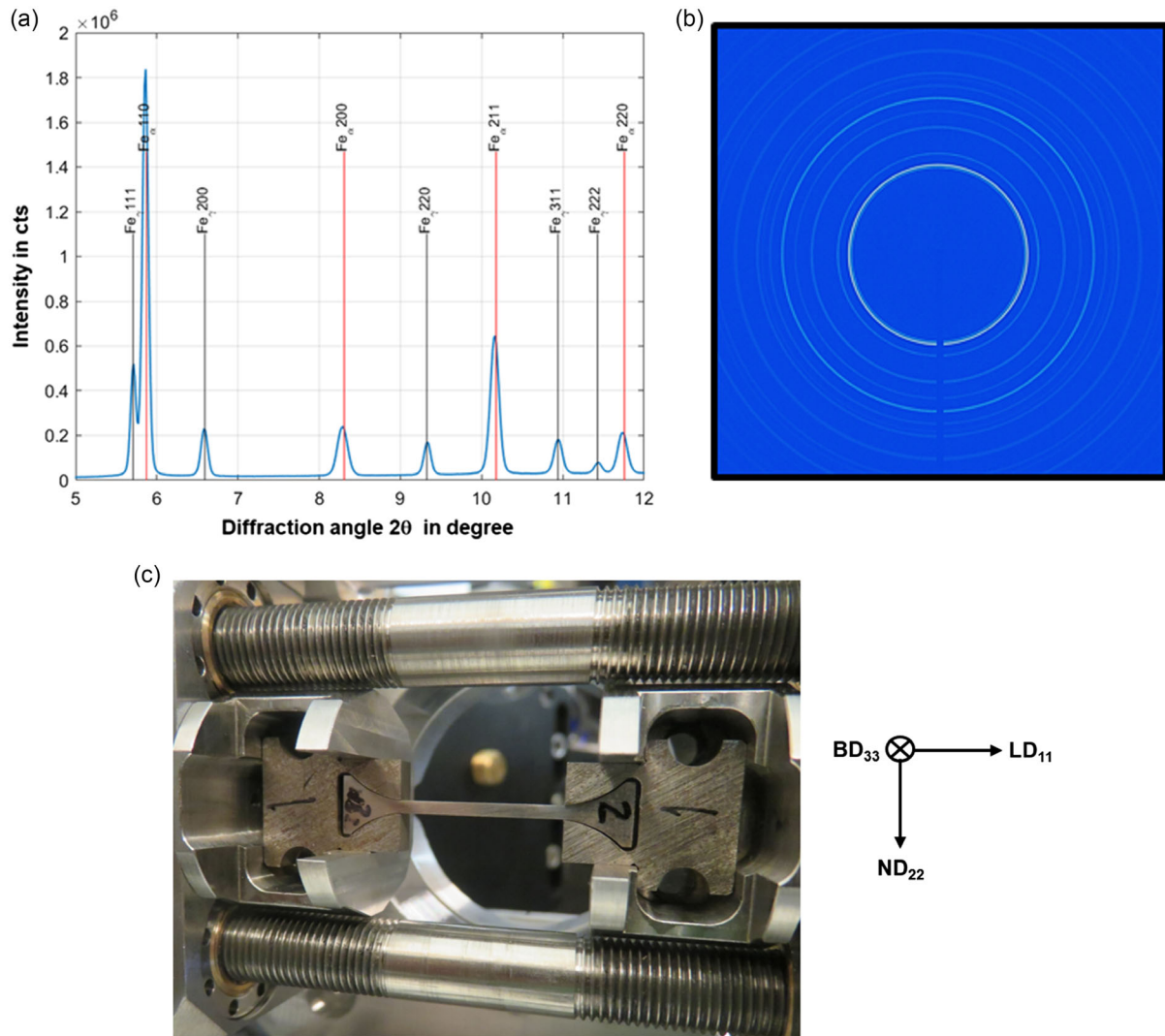
Figure 2. a) Fully integrated diffraction profile from a QP220 specimen probed using a X-ray energy of 59.718 keV, an exposure time of 1 s and a beam size of 1×1 mm^2. b) Detector image of the DSRs during loading of the specimen. c) Dog-bone-shaped specimen mounted in the stress rig under tensile load in the experimental hutch of beam line P02.1 and corresponding coordinate system indicating the LD, normal direction (ND), and synchrotron BD. The indices given are used to label the direction of the stress components in the remainder of the text.

pixels, size of 200×200 µm^2 each) was used. Prior to the analysis, the detector distance was calibrated using a LaB6 standard as well as a Python-based tool, named "pyFAI".[38,39] This program was also used in a Python script for azimuthal integration (caking) and full integration of the DSR. In order to be able to ensure a stable evaluation even with low RA contents, the mean value was taken over 10 consecutive detector images. The $\sin^2\alpha$-approach[33] was used to analyze the phase-specific stresses in LD, while the four-line method[36] was used to determine the fraction of the austenitic phase. The experimental and wavelength-dependent R-value for evaluation of RA was determined specifically for this measurement setup based on the R/R ratio assessed, taking into account the first, load-free DSR images. In this case, the RA fraction was determined using the Rietveld method and the FullProf software.[40] The integral intensities of the austenitic hkl lattice planes 200 and 220

and the martensitic/ferritic hkl lattice planes 200 and 211 (from the fully integrated DSRs) were determined for each detector image. Corresponding to the Rietveld analysis, the following R/R ratios were determined for the used wavelength: $R_{\gamma200}/R_{\alpha200} = 32.74$; $R_{\gamma220}/R_{\alpha211} = 103.9$; $R_{\gamma200}/R_{\alpha211} = 92.4$; and $R_{\gamma220}/R_{\alpha200} = 36.8$. Based on this strategy, the RA values were calculated from the integral intensity of these lattice planes during the in situ experiment. In Figure 2a the fully integrated diffraction profile, calculated based on the detector image shown in Figure 2b, is shown. The specimen considered was heat treated (condition QP220). Individual hkl indices of the lattice planes were provided. The diffraction profile only revealed the presence of fcc and bcc peaks. As a result of the high silicon content of the 42SiCr steel formation of carbides was strongly hampered.[30] The doge-bone-shaped tensile specimen mounted in the stress rig displayed in Figure 2c.

**ADVANCED
SCIENCE NEWS**

www.advancedsciencenews.com

**ADVANCED
ENGINEERING
MATERIALS**

www.aem-journal.com

Table 3. Phase specific DEC values used for stress calculation from the measured strains.

Phase	{hkl}	s_1 [Pa^{-1}]	$\frac{1}{2}s_2$ [Pa^{-1}]
bcc	110	−1.27	5.8
	200	−1.9	7.7
	211	−1.27	5.8
	220	−1.27	5.8
	310	−1.67	7.02
fcc	111	−8.4	4.31
	200	−2.91	7.53
	220	−1.35	5.86
	311	−1.93	7.6
	222	−8.4	4.31
	400	−2.91	7.53

The measuring point was located in the middle of the cross section of the specimen. Since the stress rig applies the deformation symmetrically with two crossheads running in opposite directions, it was ensured that the specimen volume to be examined always remained probed by the X-ray beam. However, since the location of the failure could also be outside of the area covered by the X-ray beam, the stress rig was stopped at regular intervals and a line scan was carried out along the sample. This procedure ensured that the specimen was always completely recorded at specific points in loading history.

2.3.2. Laboratory Experiments

All laboratory experiments were carried out in angle-dispersive mode in reflection condition with a measuring range adapted to the wavelength applied. In a first step, the RA fractions of the cylindrical specimen used for the standard tensile test (see Figure 1a) were analyzed. For this purpose, a two-cycle diffractometer manufactured by SIEMENS with a standard X-ray tube (Mo $K_{\alpha 1+2}$ radiation) was used. The primary beam path was set using a pinhole collimator with a diameter of 0.5 mm, and a secondary aperture with a width of 0.5° was applied. The specimens were scanned in a range from $2\Theta = 20°$ to $40°$ with a step size of 0.05° and a counting time of 20 s. To determine the RA content, the four-line method[36] was used following a Gaussian fit and the Rachinger separation. The diffraction lines of the 200 and 211 hkl lattice planes were taken into account for the martensite/ferrite phase, while the hkl lattice planes 220 and 311 were considered for the austenite phase. The R-values required for the evaluation were taken from literature[36] and selected as follows: For the annealed martensitic/ferrite, $R_{200} = 290$, $R_{211} = 558$ and for the austenite $R_{220} = 388$, $R_{311} = 428$. To assess the depth distribution of the RA, surface material was removed layerwise by local electrochemical polishing.

Residual stress in situ measurements under laboratory conditions were only carried out for a QP170 specimen using the geometry shown in Figure 1b. A six-circle diffractometer was used for these investigations, which was also able to support the Kammrath & Weiss miniature stress rig. This diffractometer,

Type Seifert XRD 3003 micro, was equipped with a standard tube using Co $K_{\alpha 1+2}$ radiation and a polycapillary lens with a 2 mm diameter aperture on the primary beam path and a 0.4° parallel plate collimator in front of a Li$_{200}$ monochromator on the secondary beam path.

3. Results and Discussion

3.1. Microstructure and Tensile Behavior

Microstructural analysis after the different Q&P heat treatments was carried out by EBSD in the center of cross sections. The main goal of the investigation was to understand the distribution of the RA as well as its morphology and size as will be discussed by the phase maps shown in **Figure 3**c,d. Figure 3a,b shows representative EBSD inverse pole figure (IPF) maps with superimposed image quality for both conditions, QP220 and QP170, respectively. Based on analysis of the IPF maps, first insights into microstructure evolution can be obtained with respect to grain morphology and crystal orientation. Here, irrespective of the condition, similar microstructures can be seen. Both conditions are characterized by a fine, predominantly needle-like microstructure without preferred orientation. As a result of the lower quenching temperature, an overall finer microstructure can be derived for the QP170 state. The significant impact of the different quenching temperatures is also underlined by the corresponding phase maps depicted in Figure 3c,d. In general, both conditions are characterized by a primarily martensitic microstructure (displayed in blue color) with embedded RA (yellow). However, for the QP220 condition an increased fraction of RA can be deduced. Evaluation of the EBSD measurements provides a volume fraction of RA of approximately 26% and 19% for the conditions QP220 and QP170, respectively. As the lower quenching temperature of the QP170 condition is closer to the martensitic finish temperature M_F, less of the initial austenite phase remains in the microstructure. The results shown are in absolute agreement with the Koistinen–Marburger relationship, that is, higher austenite contents can be expected with increasing quenching temperature up to the optimum quenching temperature.[13] Furthermore, differences can be seen with respect to the morphology of the RA for the both conditions considered. While the QP170 condition is characterized by a mixture of needle-like RA grains as well as some larger RA grains, which are referred to as blocky austenite according to Diego–Calderon et al.,[9] a higher fraction of blocky austenite can be observed for the QP220 state induced by the higher quenching temperature. Both morphologies have been shown in previous studies depending on different heat treatment parameters.[9,41–43] According to Diego–Calderon et al.[9] the largest blocky-type austenite grains tend to show a relatively low mechanical stability during tensile load. As a result this type of morphology transforms to martensite even under small strains and, thus, contributes only to a small extent to the TRIP effect, whereas needle-like RA grains are known to be most resistant against premature transformation.[9]

Using XRD, RA depth profiles of the cylindrical specimens (see Figure 1a) was determined under laboratory conditions in reflection mode (directly in the gauge length). At the direct
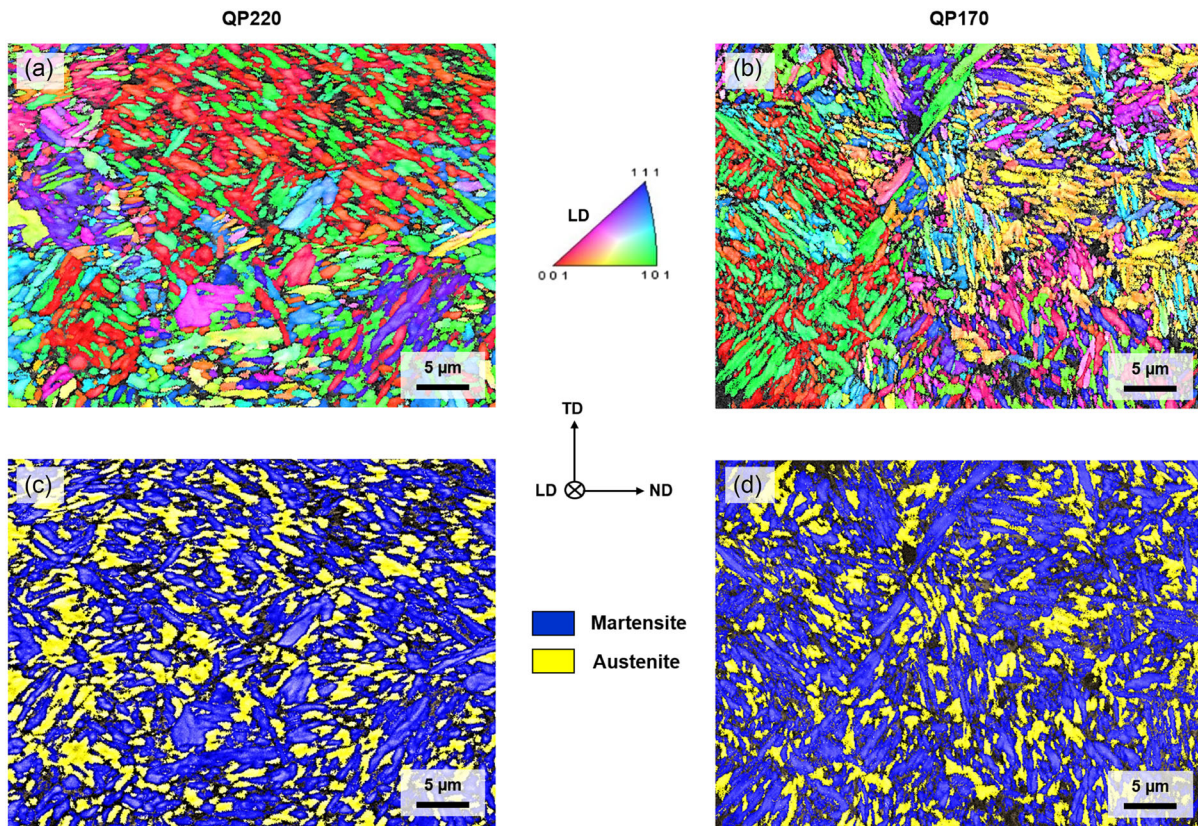
QP220   QP170

Figure 3. EBSD IPF maps with superimposed image quality of a) QP220 and b) QP170. The grain orientations are plotted with respect to the LD of the cylindrical specimens; EBSD phase maps with superimposed image quality of c) QP220 and d) QP170.
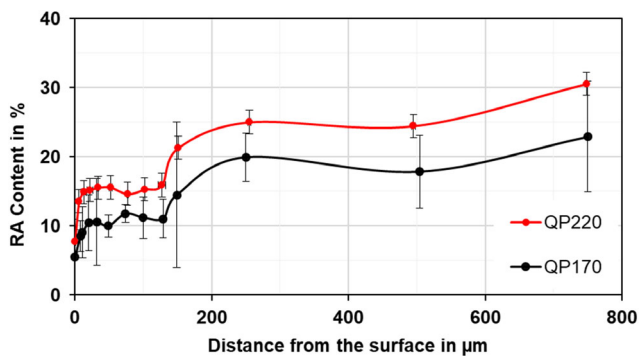

Figure 4. RA depth profile of the investigated low-alloy 42CrSi steel in QP220 and QP170 conditions.

surface of the specimens, RA contents of about 8% for the QP220 condition and 5.5% for the QP170 condition, respectively, can be determined as plotted in **Figure 4**. As expected, in this case, the RA fraction of the QP220 condition is larger compared to the QP170 counterpart. However, the absolute values appear to be significantly lower than expected. Based on the fact that decarburization effects cannot be ruled out for the surface layer, a stepwise material removal by electrochemical polishing followed by successive RA measurements was carried out up to a maximum depth of 750 μm. As a result, Figure 4 shows that the RA fraction

steadily increases with increasing removal depth. After an initial steep increase, the RA fractions of both conditions are characterized by a kind of plateau up to a depth of approximately 125 μm, indicating significant decarburization effects. With further increasing distance from the surface, the RA content increases again irrespective of the condition considered. As shown, at the maximum depth of about 750 μm, the QP170 and QP220 conditions are characterized by RA contents of about 23% and 30%, respectively. These values are in good agreement with those determined via EBSD in the center of the cross sections and illustrate that the decarburization effects, which are very pronounced in the immediate vicinity of the surface, influence the RA content down to a depth of about 750 μm. The results presented clearly show that for future investigations austenitizing should be conducted in inert gas atmosphere in order to avoid or minimize the decarburization effects observed. Generally, differences as well similarities become obvious when comparing the RA content with data reported in other studies in literature investigating similar materials (e.g., refs. [13,30]), once again pointing out the complexity of the Q&P treatment. It can thus be concluded that the RA content finally is set by the complex interplay of Q&P temperatures and times as well as the specimen geometry.

The behavior under uniaxial tensile loading, depicted in **Figure 5**a, is illustrated by representative stress–strain curves obtained for both conditions considered, that is, QP220 and QP170. The QP220 condition is characterized by a YS, ultimate
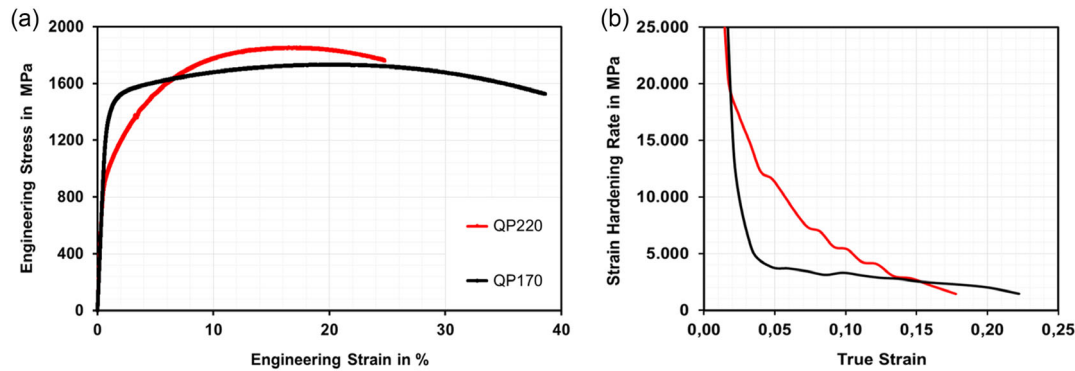
Figure 5. a) Tensile stress–strain curves and b) strain hardening rate versus true strain for representative specimens of the low-alloy 42CrSi steel in QP220 and QP170 condition.

tensile strength (UTS), and elongation to failure of approximately 850, 1850 MPa, and 24.5%, respectively. In direct comparison, an increase in YS and ductility up to about 1175 MPa and 38.5% with a concomitant decrease of UTS to about 1725 MPa can be observed as a result of the lower quenching temperature during Q&P heat treatment for the QP170 condition. The comparatively lower YS of the QP220 condition can be attributed to the lower fraction of martensite being present in the microstructure as revealed by EBSD and XRD investigations (see Figure 3 and 4). The martensite fraction mainly influences the level of the macroscopic stress states in the elastic strain region and regions of early plastic deformation.[44] After reaching the yield point, the QP220 condition is characterized by steady work hardening. On the contrary, the QP170 condition reveals an almost ideal plastic behavior. The significantly higher strain hardening capability of the QP220 condition is further stressed by the yield strength ratio of 0.47 compared to 0.67 for the QP170 counterpart. In terms of this ratio, higher strain hardening capabilities are to be expected for lower values. In line with these results, a yield strength ratio of 0.5 for a Q&P steel with a relatively high fraction of RA (>30%) is reported in ref. [13]. The high potential for strain hardening of the QP220 condition can be rationalized by the TRIP effect, that is, the strain-induced transformation of austenite grains into martensite. As a result of the higher RA fraction, the TRIP effect is significantly more effective for the QP220 as compared to the QP170 condition. According to Seo et al.[13] the kinetics of the mechanically induced martensitic transformation and the volume fraction of secondary martensite represent the key factors determining the mechanical properties. The authors report for low quenching temperatures a microstructure consisting of carbon-enriched austenite and primary martensite with low solute carbon content. High quenching temperatures were reported to lead to a microstructure consisting of an austenite phase less enriched in carbon, primary martensite with a low solute carbon content and secondary martensite with a carbon content similar to the austenite phase. The high carbon content in the RA quenched at lower temperatures leads to a high RA stability, eventually resulting in sluggish transformation kinetics. Thus, the high YS and ductility of the QP170 condition in the present study can be rationalized. In contrast, a lower RA stability due to a lower carbon content results in more rapid transformation kinetics. These rapid transformation kinetics were found to be the reason

for a higher initial work hardening rate eventually leading to a high UTS level.[13] This is in line with the results obtained for the QP220 condition in the present study and is further underlined by the strain hardening rate versus true strain curves (plotted up to the onset of necking, i.e., the point where the strain hardening rate becomes equal to the true tensile stress[45]) of the two investigated conditions shown in Figure 5b. Generally, both conditions are characterized by high strain hardening rates being in line with the results reported by Frint et al.[46] for Q&P-processed materials. Besides the carbon content, the stability of the RA is also affected by its morphology.[47] While needle and film-like morphologies are characterized by relatively high stabilities, martensitic transformation of blocky-type RA tends to take place already under small strains. As a result, this type of RA is depleted already within the early stages of deformation. Thus, this type of RA contributes to the TRIP effect (i.e., to a delay of necking at large strains) only to a small extent.[47–51] Accordingly, the blocky-type RA being present in the QP220 condition immediately transforms to martensite after reaching the yield point. Only the more stable needle-like RA transforms progressively upon initial yielding, that is, in the course of loading. In any way, the fraction of transformation-induced martensite, being different to the primary martensite in terms of its higher carbon concentration,[52,53] increases after yielding. The mechanically transformed martensite thus contributes to the final strength of the material. Based on these considerations, most pronounced hardening in the early stages of deformation, and the significantly increased UTS of the QP220 condition, can be rationalized. After reaching the onset of necking, the ductility is thought to be enhanced only by the contribution of the volume fraction of needle and film-like RA, respectively.[43] Such specific RA morphology is present in higher volume fraction in case of the QP170 condition (as demonstrated by EBSD, see Figure 3). Eventually, such microstructure appearance is considered to be the major factor to rationalize the increased elongation at fracture of the QP170 condition. However, from the results detailed so far (elaborated based on state-of-the-art ex situ assessment), it can be deduced that the RA transformation in Q&P steels is very complex and, eventually, cannot be assessed to the depth required to establish reliable process-microstructure-property relationships. As a result, the transformation kinetics will be analyzed in more detail comprising in situ approaches in the following sections.
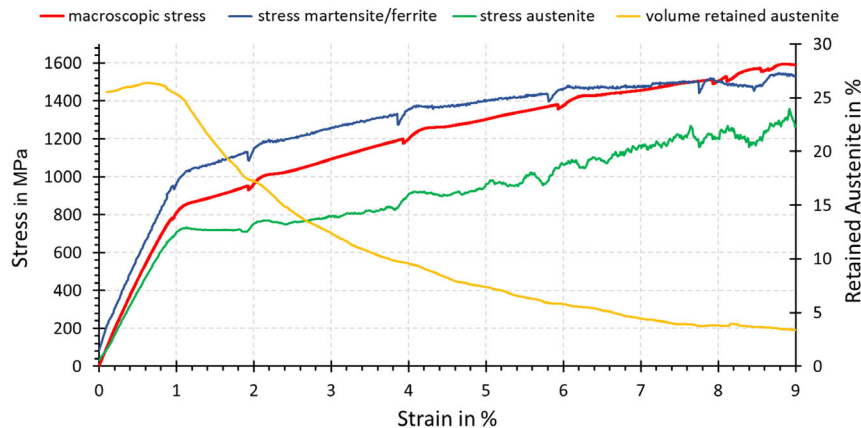
Figure 6. Tensile stress–strain curve (red, macroscopic stress) obtained from synchrotron-based in situ experiments for low-alloy 42CrSi steel in QP220 condition. Corresponding phase-specific stress–strain curves and the evolution of the RA content are plotted in blue, green, and yellow, respectively.

3.2. In Situ Analysis

3.2.1. Synchrotron Experiments

Figure 6 and **8** depict the stress–strain curves of the synchrotron-based in situ experiments. Figure 6 illustrates the behavior of the QP220 condition whereas Figure 8 refers to the QP170 condition. In addition to the macroscopic stresses displayed in red, the phase-specific stresses of the fcc and bcc phases and the RA content displayed in green, blue, and yellow, respectively, are also shown. For clarity, the corresponding curves are only plotted within the loading interval ranging from the respective yield point up to the point where a RA content close to the detection limit of about 2% prevails. Based on the analysis of this specific interval, the most important microstructural and mechanical characteristics of the two conditions considered can be assessed. However, it has to be noted that after failure the specimens of both conditions still feature RA content of approximately 2%. In line with literature this can be attributed to the hydrostatic pressure related to the high martensite volume fraction. As a result of this hydrostatic pressure, the strain-induced phase transformation is suppressed leading to higher austenite stability.[19] The phase-specific residual stresses (unloaded state) of both phases considered are on a relatively low level in both the QP220 or the QP170 condition and, thus, are considered negligible. Based on a direct comparison of the initial RA fraction seen here and the values previously determined using EBSD and XRD (in the center of the specimen), it becomes obvious that these are in good agreement. It is important to note at this point that the synchrotron analysis provides bulk information of the specimens. As detailed in Section 2, the stress rig was stopped at regular intervals and line scans were carried out along the specimen for all in situ measurements shown in the present study. Stress relaxation occurred during each interruption of the tensile tests. The slight increase in the stress values seen as a result of the stops can be attributed to the control algorithm of the stress rig, but will not be discussed for the sake of brevity. A similar behavior was already shown by Kromm et al.[34] for in situ interrupted tensile tests focusing on a high-strength TRIP steel. The phase-specific stresses of both conditions increase upon loading in accordance to the macroscopic stresses in the elastic regime. Looking at the details presented in Figure 6, the RA content of the QP220 condition seems to increase in the elastic region. This observation might be attributed to the annihilation of dislocations in the RA. As a result, the diffracting volume (domain size) of the RA increases. This observation is further underlined by **Figure 7** displaying an enlarged and, thus, more detailed view on the evolution of the RA fraction in the area in focus. Here, the integral width of the RA diffraction peak of *hkl* lattice plane 311 is shown in addition. From the results presented it becomes obvious that an abrupt change in the integral width correlates with the maximum of the RA fraction curve (indicated by the blue dashed line in Figure 7). The integral width under constant experimental conditions is a measure for the microscale residual stresses and, thus, a comparative measure for plastic deformation and dislocation density, respectively. Thus, an annihilation of dislocations in the RA can be deduced from detailed analysis of Figure 7.
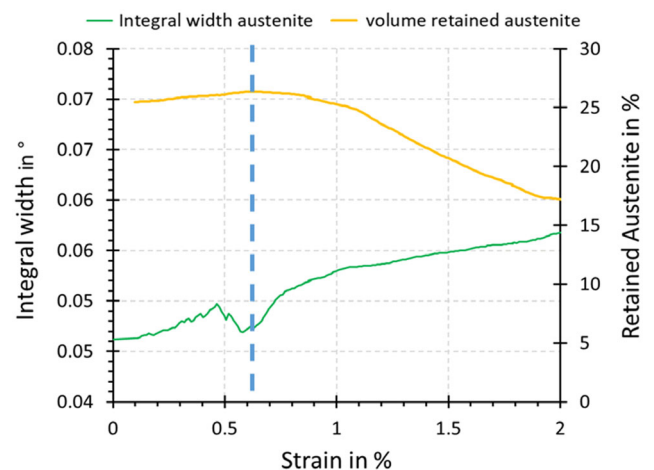

Figure 7. Detailed view of the evolution of the RA volume fraction and the integral width of the 311-lattice plane for the low-alloy 42CrSi steel in QP220 condition. See text for details.

After passing the yield point, the RA content of the QP220 condition (see Figure 6) decreases continuously before a plateau evolves, that is, a saturation of the fraction of RA prevails at an elongation of about 7.5% (the fraction of austenite being close to the resolution limit of the approach considered). Moreover, based on the slope, that is, the kinetics of the transformation, the curve can be segmented into different regimes. Such a fact directly pinpoints different stabilities of the RA fractions being present (i.e., RA of different morphology, see Figure 3). As shown by the EBSD measurements in Figure 3, the RA in the QP220 condition is characterized by a relatively high fraction of blocky austenite. According to Diego-Calderon et al.,[9] this type of austenite is characterized by an inferior mechanical stability during tensile load and, thus, transforms to martensite already under very small strains. Eventually, such kind of RA only contributes to a small extent to the TRIP effect upon additional plastic deformation. From the evolution of the RA fraction displayed in Figure 6 the same conclusions can be drawn. After transformation of the blocky RA, the remaining RA is only composed of the needle-like austenite grains, which are known to be more resistant against premature transformation.[9] For this reason, a change in the course of the slope of the RA curve is seen. These considerations are further supported by the development of the phase-specific stress of the austenite. As can be derived from Figure 6, after yielding the stress–strain curve of the austenite is characterized by an almost horizontal course, eventually revealing the inferior mechanical stability and rapid transformation kinetics of the blocky austenite. Hardly any traces of hardening can be seen. After reaching a strain of approximately 2%, the stress in the austenitic phase continuously increases. This finding reveals two important aspects: the blocky austenite already fully transformed to martensite and strain hardening in the remaining needle-like austenite sets in due to the resistance of these grains against strain-induced transformation. The observations made can moreover be correlated to the strain-hardening behavior evaluated from the tensile tests conducted using the cylindrical specimens (see Figure 5). Figure 5b clearly reveals that a change in the strain hardening behavior of the QP220 condition takes likewise place at an elongation of about 2–2.5% strain. After reaching this point the

condition is characterized by a different slope of the work hardening curve. The QP220 condition is generally characterized by rapid transformation kinetics. This can be expressed based on calculation of the rate of transformation for a given interval. In the range between 1% and 4% strain, the QP220 condition is characterized by a transformation rate of about 5% RA/1% strain.

A different transformation behavior of the QP170 condition can be derived from the evolution of the RA displayed in **Figure 8**. As the microstructure of the QP170 condition predominantly is characterized by needle-like austenite grains and only features blocky-type RA of very low fraction, the transformation kinetics in the very early stages of deformation generally are sluggish compared to the QP220 condition. For the discussion in the remainder of this section, it is important to note that a very distinct feature of the QP220 condition is not seen in case of the QP170 condition: A plateau-like stage up to a strain level of 0.7% (see Figure 7 for the QP220 condition) is not present, further pointing at the significant differences in terms of the elementary characteristics, for example, the dislocation density, of the RA formed upon different Q&P treatments. The changes in transformation kinetics become most obvious after calculation of the transformation rate. In the interval between 0% and 4% strain, a transformation rate of about 2.5% RA/1% strain is deduced, this value being only half the rate found for the QP220 condition in the same strain interval. Thus, the significant influence of the different RA morphologies on the transformation characteristics of the two conditions considered is clearly proven. Upon reaching a total strain of about 5%, the transformation behavior of the QP170 condition changes. In the following, the continuous decrease of the RA is interrupted by several abrupt drops pointing at a Lüders-like behavior. As exemplarily shown by the dashed grey line, these drops occur during stages of continuous load increase (i.e., not during the stops of the tests implemented for probing the entire gauge section, see Experimental Section). Thus, it can be concluded that these drops are not related to those stops. In all cases, a small decrease in the stress level of the austenite phase can be observed before spontaneous decrease of the RA fraction. In conclusion, a rapid, avalanche-like strain-induced transformation of the RA sets in. This
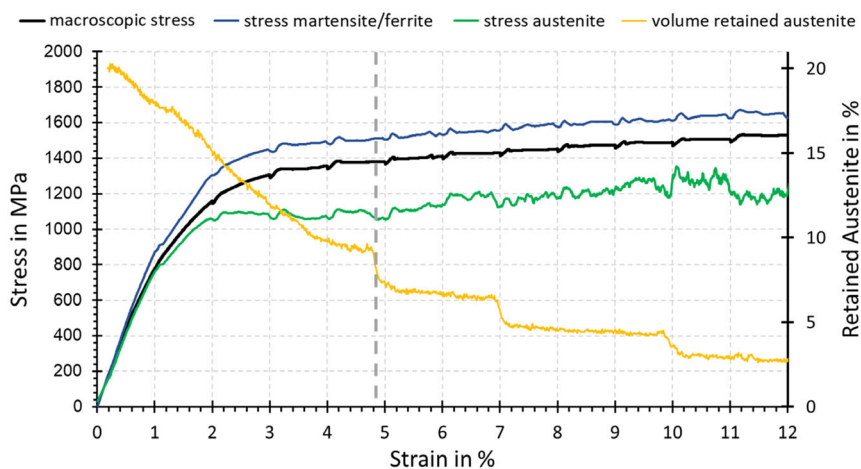

Figure 8. Tensile stress–strain curve (black, macroscopic stress) obtained from synchrotron-based in situ experiments for low-alloy 42CrSi steel in QP170 condition. Corresponding phase-specific stress–strain curves and the evolution of the RA content are plotted in blue, green, and yellow, respectively.

**ADVANCED
SCIENCE NEWS**

www.advancedsciencenews.com

**ADVANCED
ENGINEERING
MATERIALS**

www.aem-journal.com

characteristic transformation event is indicated by a decrease of the residual stress level in the austenitic phase before (Figure 8). A model introduced in ref. [11] revealed that the carbon content of the RA increases with decreasing quenching temperatures. Furthermore, it was numerously observed that the carbon content of the RA significantly affects the behavior and stability of the microstructure during external loading.[13,52] Based on these facts an influence of the carbon content on the Lüders-like behavior could be expected and, indeed, is seen here, but only for the QP170 condition. This observation might likewise be in line with the results of Min et al.[18] reporting that the carbon concentration is relatively high in small grains, such as the RA grains with needle-like morphology, due to the overall smaller grain volume. However, in order to further evaluate the influence of the carbon content on the differences in the RA transformation behavior, further aspects need to be considered. These aspects will be discussed in Section 3.2.2.

Differences in the two heat treatment conditions considered can also be observed by direct comparison of the phase specific stress–strain curves of the martensitic phase. As can be derived from Figure 8, for the entire area shown the martensitic stress curve of the QP170 condition displayed in blue is located above the macroscopic stress. This observation likewise only holds true for the QP220 condition at early and medium stages of deformation (see Figure 6). Upon reaching a strain of approximately 5–6%, the martensitic stress curve continuously starts to slope down until an intersection with the macroscopic stress occurs at about 8% strain. The differences seen can be rationalized based on the well-known Masing model.[54,55] In this model, a quasi-isotropic metal consists of a number of volume elements of different yield strengths (referred to as component in the following), some of which are well above the experimentally determined YS of the entire specimen. Furthermore, all components are assumed to be ideal-plastic. According to the Masing model, each component in the undeformed state is deformed elastically upon initial loading until the weakest component reaches its yield point. In the further course of deformation, the stronger component is responsible for carrying the load since the weaker element does not longer contribute to an increase in the macroscopic stress. After reaching the yield point of the stronger component, the entire specimen starts to deform ideal-plastic. In case of the present study, the RA represents the weaker component whereas the martensitic phase is the stronger component. Accordingly, solely the RA is deformed plastically after reaching the macroscopic yield point (at this point the concomitant hardening response related to the TRIP effect is neglected for simplicity). As a result, the martensitic phase is only elastically deformed, which presumably results in a constant course of the phase specific martensite curve above the macroscopic stress as seen for the QP170 condition. In direct comparison, it can be deduced that the decrease of the martensitic stress curve seen in case of the QP220 condition indicates the onset of plastic deformation of the martensite. The different behavior of both conditions can be rationalized by the different strength of the respective martensite being present. As expected (lower C contents in the primary martensite were shown for higher quenching temperatures in ref. [13]), the martensite formed during the Q&P treatment in case of QP220 seems to be characterized by a lower strength (i.e., a lower C content) compared to the QP170 counterpart. However, in order to evaluate these considerations experimentally, further investigations supported by micromechanical testing of the different martensite phases need to be conducted. These will be subject of future studies.

3.2.2. The Lattice Distance of the Strain-Free Orientation versus Local Chemical Composition

It is well documented in literature[56] that the stress-free lattice distance $D_{0, hkl}$ needs to be known to assess a three dimensional stress state $\overline{\sigma}_{11} \neq \overline{\sigma}_{22} \neq \overline{\sigma}_{33}$. Here the major problem is that the $D_{0, hkl}$ value is influenced by the local chemical composition of the alloy and an exact value needs to be calculated or determined each time. In case of an in-plane stress state, that is, $\overline{\sigma}_{33} = 0$, the stress-free lattice distance $D_{0, hkl}$ is equal to the strain-free lattice distance D_{hkl}^* corresponding to the strain-free direction ψ^*.[56] In accordance with the phase-specific element unit cell a corresponding a^* value can be calculated of each D_{hkl}^* from the phase considered. Vice versa a difference between the overall $D_{0, hkl}$ and D_{hkl}^* pinpoints the presence of a stress component $\overline{\sigma}_{33} \neq 0$ or a variation in the chemical composition.[56] Considering the experimental conditions being the basis of the present study, the exact residual stress situation in the probed phases cannot be calculated due to two reasons: the missing $D_{0, hkl}$ values as well as the fact that the specimen was not rotated during the in situ measurements (to characterize two different stress directions). Nevertheless, due to the fact that the exact loading condition and the stress differences between two load steps (of several loading sequences) are known, it can be stated that the stresses in LD most effectively are increased. In contrast, the transversal directions, which are only influenced by the transversal contraction, are hardly affected.

In line with the boundary conditions of the measurement and stress evaluating method applied[33] (see Section 2.3), the mean value of the initial residual stress state in beam direction and specimen thickness, respectively, is equal to zero, while the stress components σ_{22} and σ_{33} are only influenced by the transversal contraction strain upon increasing the load. As a result, the stress components σ_{22} and σ_{33} are considered to be equal for every load step, and the difference of both components is thus equal to zero. This fact opens the opportunity to calculate the D_{hkl}^* value from the linear fitted function D_{hkl} against $\sin^2\psi$ taking into account the corresponding strain-free direction $\sin^2\psi^*$ evaluated based on the equation for Case I listed in **Table 4**.

The equations for the strain-free directions of both cases, shown in Table 4, assume that the DEC values s_1^{hkl} and $\frac{1}{2} s_2^{hkl}$ are exactly known. Generally, this fact represents another weak

Table 4. Equations used to calculate the strain-free direction $\sin^2\psi^*$ for the two different stress states considered.[56]

Case	Stress state	Strain free direction
I	$\overline{\sigma}_{11} \neq \overline{\sigma}_{22} = \overline{\sigma}_{33} = 0 \quad \varphi = 0°$	$\sin^2\psi^* = -\dfrac{s_1}{\frac{1}{2}s_2}$
II	$\overline{\sigma}_{11} = \overline{\sigma}_{22} \neq \overline{\sigma}_{33} = 0 \quad \varphi = 0°$	$\sin^2\psi^* = -2\dfrac{s_1}{\frac{1}{2}s_2}$

ADVANCED
SCIENCE NEWS

www.advancedsciencenews.com

ADVANCED
ENGINEERING
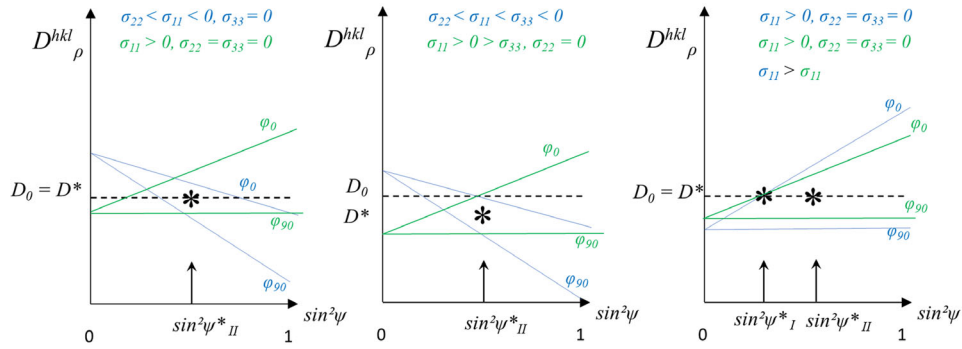**MATERIALS**

www.aem-journal.com

Figure 9. Schematic detailing the strain distribution as a function of $\sin^2\psi$ for two different stress states. The possible behavior of the strain-free direction equal and unequal to D_0 is highlighted. Recompiled for transmission mode from ref. [56].

point of the approach. However, this can be circumvented in an in situ experiment: For assessment of ex situ experiments, DEC values are crucially needed to calculate the unknown residual stress states based on the experimentally determined strains. However, in case of in situ measurements, the macroscopic (load) stress corresponding to the experimentally determined strains can be directly deduced from experimental data available. Considering the boundary conditions prevailing in the present study, the question is to be answered if the values $D_{hkl}*$ and the corresponding $\sin^2\psi*$ coincide with the crossing point between the D_{hkl} against $\sin^2\psi$ linear-fitted function of different load levels (**Figure 9** illustrated for transmission mode).

This behavior can be evaluated by plotting these linear functions for the initial elastic load levels. **Figure 10** and **11** depict these plots for the 211 and 311 hkl lattice planes of the martensite/ferrite and austenite phases, respectively, for each heat treatment condition considered. In Figure 10a and 11a the D_{211} against $\sin^2\psi$ linear fitted functions of the heat-treated conditions QP170 and QP220, respectively, show an obvious crossing point, corresponding to Case I listed in Table 4.

While the intersection points in Figure 10a and 11a are almost in perfect agreement with the theoretical $\sin^2\psi*$ Case I (only showing slight deviations, see magnified views of the intersection points given in Figure 10c and 11c), the intersection points of the 311
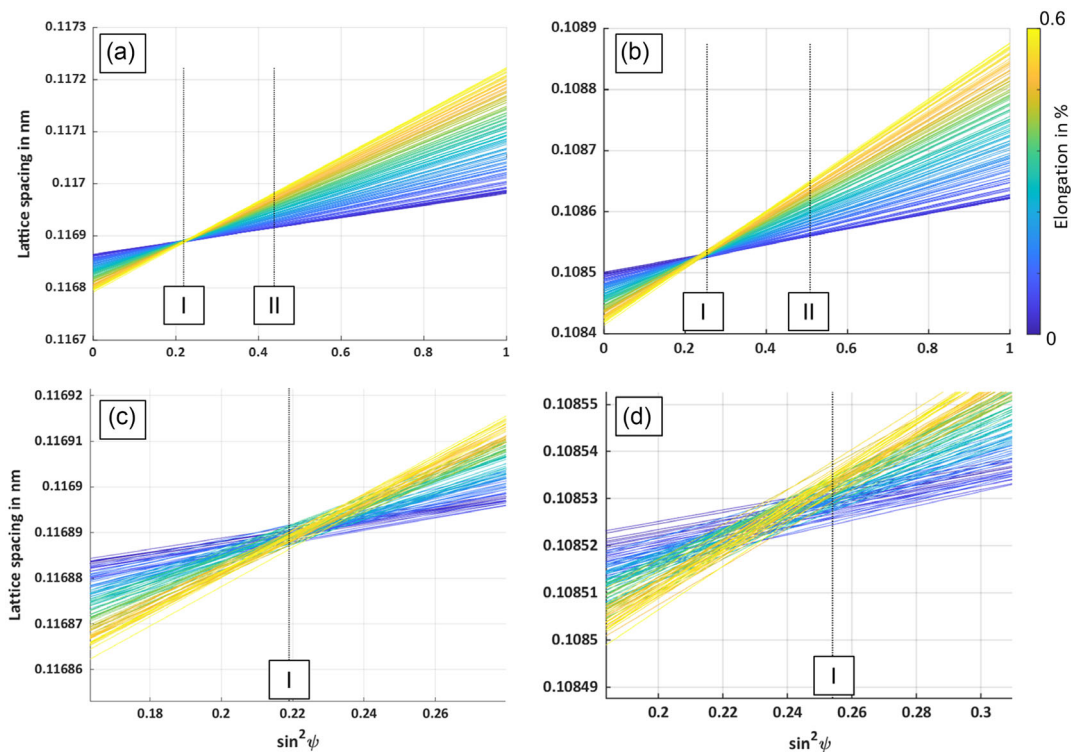

Figure 10. Graphical analysis of the intersection points between the D_{hkl} against $\sin^2\psi$ linear fitted functions for different load levels (from 0% to 0.6%) in the elastic regime of the QP170 condition: a) martensite/ferrite 211 lattice plane and b) austenite 311 lattice plane. Subfigures c) and d) show the enlarged views of the intersection points in (a) and (b).
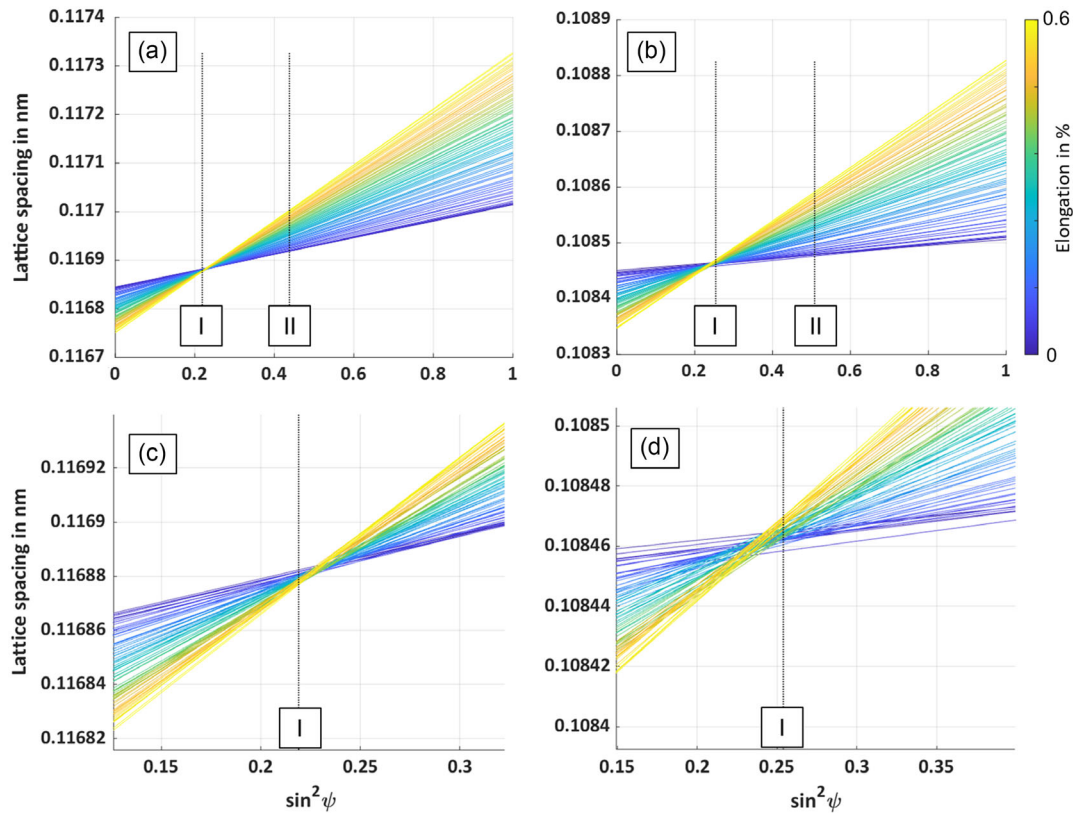
Figure 11. Graphical analysis of the intersection points between the D_{hkl} against $\sin^2\psi$ linear fitted functions for different load levels (from 0% to 0.6%) in the elastic regime of the QP220 condition: a) martensite/ferrite 211 lattice plane and b) austenite 311 lattice plane. Subfigures c) and d) show the enlarged views of the intersection points in (a) and (b).

lattice plane in Figure 10b and 11b are slightly shifted toward lower and higher values, respectively, as shown in Figure 10d and 11d. Such slight deviations are thought to be absolutely reasonable as the DECs applied (see Table 3) might not exactly fit the elastic behavior of the austenite phase established by the Q&P heat treatment conditions in focus, that is, QP220 and QP170.

By calculating the mean value of all intersection points for all different load levels, $D_{hkl}*$ can be evaluated. This is done in **Table 5** for the 311 austenite lattice plane. This value is then directly compared with the theoretical $D_{0,\ hkl} = D_{hkl}*$ for the stress condition $\overline{\sigma}_{33} = 0$.

As the experimental conditions and the load situations were the same, the differences of the $D_{311}*$ values of the two different heat treatment conditions, that is, QP170 and QP220, can be rationalized by different carbon contents in the austenite unit cell. In the QP170 condition, characterized by the lower RA

fraction, the austenite only provides less volume to absorb the carbon. In line with this consideration, the carbon content in the unit cell of the QP170 condition is expected to be higher as compared to the unit cell of the QP220 condition, which is in agreement with data reported in literature.[11] It can thus be assumed that this higher content of carbon after an initial continuous transformation of larger RA grains with less stability at early-to-medium stages of deformation results in the Lüders-like pinning effect of dislocation movement as revealed for the QP170 condition in Figure 8. By this pinning effect the ductility of the austenitic grains in the elastic-plastic region of the stress–strain curve is reduced. As the martensitic phase is only deformed elastically (see explanation by Masing model) for proceeding macroscopic deformation and TRIP, a critical stress state is needed to overcome the pinning effect of the dislocation movement. This effect eventually explains the abrupt drops in the RA content of the QP170 condition.

Despite differences in the transformation behavior of the RA, both conditions revealed similar RA volumes toward the end of the tensile test. This can be attributed to the pronounced stability of the strain-free direction, which is characterized by a low scatter at the intersection point of the strain lines (see Figure 10 and 11). Due to an insufficient strain in this direction, no transformation of the RA takes place, thus explaining the remaining RA content of both conditions toward the end of the tensile test. This is in line with the observations reported in refs. [24,57]. Investigating

Table 5. Theoretical and calculated $D_{311}*$ values as well as corresponding unit cell length $a_{fcc}*$ taking into account the crossing points of the different load levels. The theoretical value $D_{0,\ hkl} = D_{hkl}*$ corresponds to the stress state $\overline{\sigma}_{33} = 0$.

Value	Theory [nm]	QP170 [nm]	QP220 [nm]
$D_{311}*$	0.10827	0.108526	0.108461
$a_{fcc}*$	0.35909	0.35994	0.35972

the interplay between martensite formation, texture evolution, and load partitioning in low-alloyed TRIP steels Jimenez-Melero et al.[57] showed a significant fraction of untransformed austenite at fracture of the specimen for two different TRIP steel conditions. Furthermore, in their study investigating the martensitic transformation in Q&P steels, Finfrock et al.[24] reported on untransformed RA in the neck of the specimen after fracture. Eventually, the results presented in these studies can be explained by the absent RA transformation in the strain-free direction. Untransformed RA fractions due to pronounced stability of the strain-free direction also indicate a texture development in the austenite phase during deformation. This statement is in turn supported by the results in ref. [57] revealing an evolution in texture in the austenite phase upon tensile loading. Generally, texture evolution as well as the influence of crystallographic orientation on the transformation stability of the RA are of high importance. Thus, investigations of related phenomena, for example, by in situ EBSD measurements, will be subject of future work.

3.2.3. Laboratory Experiments

Since the synchrotron experiments shown and discussed before are associated with an extremely high experimental effort and since no permanent access to beamlines is available, the knowledge gained from the experiments is used to qualify similar experiments under laboratory conditions. As a result, and as basis for future work, an in situ experiment was conducted on the specimen with the higher yield point, that is, QP170, using laboratory XRD equipment only. The measurements were carried out using the same specimen geometry (see Figure 2b)). In the same way as Figure 6 and 8, **Figure 12** shows a superposition of the macroscopic stress–strain distribution and the phase-specific stress–strain distributions of the austenite and martensite/ferrite phases as well as the related RA content.

As shown in Figure 12, a different initial RA content of approximately 14% as compared to the synchrotron experiment ($\approx$20%, see Figure 8) can be seen. This fact can be rationalized by the surface state of the specimen in combination with the

measurement setup of the laboratory experiment applied. As the specimen was ground to 5 μm grit size (see section 2.3), a mechanically induced phase transformation of the RA probably occurred in the near surface volume of the specimen. While the laboratory test experimentally determines the stress state in the surface area ($\sigma_{11} - \sigma_{33}$) in reflection mode, the synchrotron setup probes the inner specimen volume in transmission mode ($\sigma_{11} - \sigma_{22}$). The bulk material is not influenced by the specimen preparation in case of both in situ experiments. In addition, differences between the two setups considered can be seen in the evolution of the RA at the early stages of deformation. While transformation of the RA in the synchrotron experiments immediately starts upon external loading, the RA probed in reflection mode is characterized by a plateau with only slight deviations up to a strain of approximately 1.5–1.75%. At this point, yielding is obvious from the macroscopic stress curve displayed in black. Upon further increase of the load, a continuous decrease of the RA fraction can be observed. This behavior can be rationalized by the differences in the measured phase-specific stresses (green for austenite and blue for martensite). As shown, initially both phases are characterized by compressive residual stresses. Due to the fact that only surface measurements are considered in Figure 12, it can be stated that these residual stresses originate from specimen preparation, that is, grinding of the specimen. It can further be concluded that the superposition of these compressive residual stresses and the loading stresses are not sufficient to promote RA transformation directly in the very early stages of deformation. Eventually, this indicates that a controlled surface conditioning, that is, establishing compressive residual stresses by mechanical surface treatments, for example, realized by shot peening or deep rolling, can be exploited to stabilize the RA in the near surface area. This might be beneficial for cyclic properties of Q&P steels in the high-cyclic-fatigue regime. Upon initiation of the RA transformation, however, the QP170 condition is characterized by a transformation rate of about 3% RA/1% strain in the interval of 2% and 4% strain under laboratory conditions. These values are indeed similar to the results obtained by the synchrotron measurements shown in the section before and, thus, reveal a good correlation between
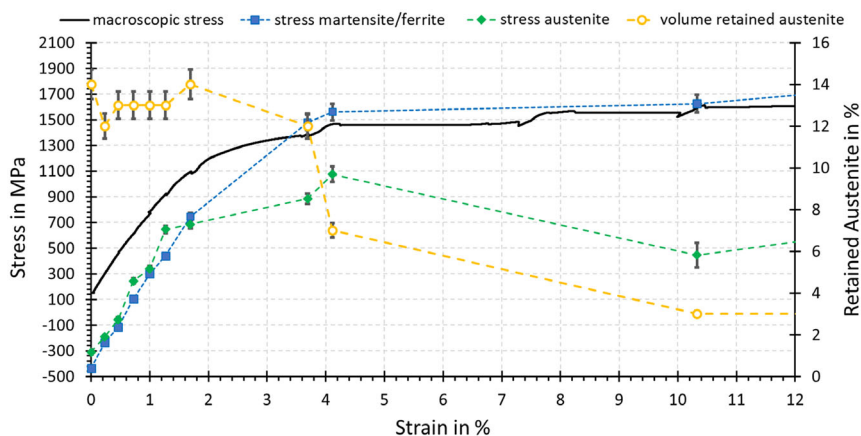

Figure 12. Tensile stress–strain curve (black, macroscopic stresses) obtained from X-ray-based in situ laboratory experiments for low-alloy 42CrSi steel in QP170 condition. Corresponding phase-specific stress–strain curves and the evolution of the RA content are plotted in blue, green, and yellow, respectively.

**ADVANCED
SCIENCE NEWS**

www.advancedsciencenews.com

**ADVANCED
ENGINEERING
MATERIALS**

www.aem-journal.com

both measurement setups. Nevertheless, it is more difficult to interpret the laboratory data in the same quality as the experiments done in transmission mode due to the small number of measurements and, thus, sampling points in the course of the curve. Due to the enormous time required for the laboratory experiment, the number of measurements needed to be limited, eventually resulting in a lack of temporal resolution. This is moreover underlined by the course of the evolution of the RA fraction at higher stages of deformation. Here, the Lüders-like behavior seen at medium-to-high degrees of deformation (>4% strain), being attributed to the higher content of carbon in the austenite unit cell of the QP170 condition (see Figure 8), is not resolved by the data obtained in the laboratory experiments. Additionally, further differences are revealed by the phase-specific stresses shown in Figure 12. In contrast to the synchrotron experiment, where the martensitic stress curve is above the macroscopic stress for the entire area shown, the stress of the martensitic phase is below the macroscopic stress in the laboratory experiments. This is thought to be a result of the high initial (compressive) residual stress state of the martensite. However, after reaching a point of intersection of the two curves at a strain of about 3.5%, the stress in the martensitic phase is constantly higher as compared to the macroscopic stress, in line with the data shown in Figure 8. Another common feature of the two datasets is that the curve of the austenitic phase is always below the macroscopic stress and the stress level of the martensite. However, as a result of the initial compressive residual stress state it is also lowered in terms of the absolute values of the stresses shown in Figure 8. Finally, after an initial increase of the phase-specific stress of the austenite up to a strain of ≈4%, the stress decreases concomitantly to the significant reduction of the RA fraction. This observation might be attributed to an evolving hydrostatic pressure as described by Hidalgo et al.[19] As the immediate formation of the martensite entails an expansion in volume, residual stresses arise as long as deformation cannot sufficiently be accommodated in the entire surrounding microstructure. It is assumed that the residual stresses minimize the phase-specific stress in the austenite phase, especially in the (relatively small) measuring volume of the near-surface layer being in focus of the laboratory experiment in reflection mode. Comparing the investigations in the surface area $(\sigma_{11} - \sigma_{33})$ in reflection mode with those in the volume obtained by synchrotron measurements for the same heat treatment condition (QP170), it becomes obvious that after passing the yield point the RA transformation as well as the evolution of the phase specific stress generally tend to behave similarly with increasing load. It can thus be confirmed that a general assessment of the stress and strain-induced transformation behavior can be obtained by the laboratory tests. However, as has been pointed out, the material in focus is characterized by a high sensitivity to surface preparation indicating that in addition to the results obtained by in situ synchrotron experiments further surface-sensitive measurements need to be conducted in future studies in order to resolve the transformation behavior in laboratory measurements even more precisely. In this context, despite the quite promising results using the laboratory setup, the temporal resolution should also be adjusted in further investigations.

4. Summary and Conclusion

In this study, the stability of RA of a low-alloy 42CrSi Q&P steel was investigated for two heat treatment conditions, differing in their initial RA content. In addition to microstructure investigations using EBSD and XRD as well as macroscopic tensile tests, complex in situ stress–strain tests with RA measurements were carried out using synchrotron as well as laboratory setups. From the findings presented the following conclusions can be drawn.
1) As a result of the different quenching temperatures, the two conditions considered are characterized by different RA contents, that is, approximately 30% for the QP220% and 20% for the QP220 condition, respectively. Comparable RA content values were determined by EBSD, XRD, as well as phase analysis based on synchrotron measurements.

2) Differences in the RA content become evident under monotonic tensile loading. While the condition with the lower RA content is characterized by a significantly higher yield point (1175 MPa) and almost ideal-plastic behavior, the condition with a higher RA content is characterized by a lower yield point (850 MPa), strong work hardening, and lower elongation at break.

3) Differences in transformation kinetics can be explained by different morphologies of the RA, that is, blocky-type austenite being characterized by a low stability as well as needle-like grains featuring a high resistance against strain-induced transformation. Generally, evolution of the phase specific stresses can be explained by the well-known Masing model.

4) After continuous RA transformation at early and medium stages of deformation, the RA content of the QP170 condition is characterized by a Lüders-like transformation behavior being attributed to pinned dislocation movements by a higher carbon content in the RA unit cells as determined by in situ synchrotron experiments.

5) A major challenge of the laboratory-based analysis strategy is the low density of measurement points and thus, a lack of temporal resolution. Nevertheless, a first correlation of results was shown for the RA stability revealing that the results obtained by the in situ synchrotron experiments can be used to qualify less-expensive laboratory XRD methods.

Conflict of Interest

The authors declare no conflict of interest.

Data Availability Statement

The data that support the findings of this study are available from the corresponding author upon reasonable request.

[1] Z. Li, K. G. Pradeep, Y. Deng, D. Raabe, C. C. Tasan, *Nature* **2016**, *534*, 227.

[2] Y. Wei, Y. Li, L. Zhu, Y. Liu, X. Lei, G. Wang, Y. Wu, Z. Mi, J. Liu, H. Wang, H. Gao, *Nat. Commun.* **2014**, *5*, 3580.

[3] J. Wang, Y. Li, G. Hu, M. Yang, *Rev. Appl. Sci.* **2019**, *9*, 5322.

[4] W. Zhang, J. Xu, *Mater. Des.* **2022**, *221*, 110994.

[5] H. E. Friedrich, *Adv. Eng. Mater.* **2003**, *5*, 105.

[6] N. Fonstein, in *Advanced High Strength Sheet Steels: Physical Metallurgy, Design, Processing, And Properties*, 1st ed., Springer, Cham **2015**.

[7] R. Kuziak, R. Kawalla, S. Waengler, *Arch. Civil Mech. Eng.* **2008**, *8*, 103.

[8] D. K. Matlock, J. G. Speer, in (Eds: A. Haldar, S. Suwas, D. Bhattacharjee), Springer, London **2009**, pp. 185–205.

[9] I. de Diego-Calderón, P. Rodriguez-Calvillo, A. Lara, J. M. Molina-Aldareguia, R. H. Petrov, D. de Knijf, I. Sabirov, *Mater. Sci. Eng. A* **2015**, *641*, 215.

[10] A. Weidner, in *Deformation Processes In TRIP/TWIP Steels* (Ed: A. Weidner), Springer International Publishing, Cham **2020**, pp. 71–98.

[11] J. Speer, D. K. Matlock, B. C. de Cooman, J. G. Schroth, *Acta Mater.* **2003**, *51*, 2611.

[12] M. Droste, M. Wendler, O. Volkova, H. Biermann, *Adv. Eng. Mater.* **2019**, *21*, 1800732.

[13] E. J. Seo, L. Cho, Y. Estrin, B. C. de Cooman, *Acta Mater.* **2016**, *113*, 124.

[14] O. Bouaziz, S. Allain, C. P. Scott, P. Cugy, D. Barbier, *Curr. Opin. Solid State Mater. Sci.* **2011**, *15*, 141.

[15] I. Sabirov, M. J. Santofimia, R. H. Petrov, *Metals* **2021**, *11*, 1419.

[16] S. Härtel, B. Awiszus, M. Graf, A. Nitsche, M. Böhme, M. F.-X. Wagner, H. Jirkova, et al., *Metals* **2019**, *9*, 577.

[17] M.-M. Wang, C. C. Tasan, D. Ponge, A. Kostka, D. Raabe, *Acta Mater.* **2014**, *79*, 268.

[18] J. Min, L. G. Hector, L. Zhang, J. Lin, J. E. Carsley, L. Sun, *Mater. Sci. Eng. A* **2016**, *673*, 423.

[19] J. Hidalgo, K. O. Findley, M. J. Santofimia, *Mater. Sci. Eng. A* **2017**, *690*, 337.

[20] P. J. Jacques, F. Delannay, J. Ladrière, *Trans. A* **2001**, *32*, 2759.

[21] B. Fultz, J. I. Kim, Y. H. Kim, H. J. Kim, G. O. Fior, J. W. Morris, *Trans. A* **1985**, *16*, 2237.

[22] B. Fultz, J. W. Morris, *Trans. A* **1985**, *16*, 2251.

[23] C. B. Finfrock, A. J. Clarke, G. A. Thomas, K. D. Clarke, *Metall. Mater. Trans. A* **2020**, *51*, 2025.

[24] C. B. Finfrock, B. Ellyson, C. G. Becker, J. Copley, K. Fezzaa, N. Parab, T. Sun, C. Kirk, N. Kedir, W. Chen, A. Clarke, K. Clarke, *Metall. Mater. Trans. A* **2022**, *53*, 3528.

[25] C. Garcia-Mateo, F. G. Caballero, J. Chao, C. Capdevila, C. Garcia de Andres, *J. Mater. Sci.* **2009**, *44*, 4617.

[26] H. Jirková, L. Kučerová, B. Mašek, *Mater. Today: Proc.* **2015**, *2*, S627.

[27] M. Kroll, P. Birnbaum, J. Zeisig, V. Kraeusel, M. F.-X. Wagner, *Metals* **2019**, *9*, 716.

[28] H. Jirková, K. Opatová, Š. Jeníček, L. Kučerová, *IOP Conf. Ser.: Mater. Sci. Eng* **2020**, *723*, 12012.

[29] A. Gokhman, Z. Nový, P. Salvetr, V. Ryukhtin, P. Strunz, P. Motyčka, J. Zmeko, J. Kotous, *Materials* **2021**, *14*, 1445.

[30] I. Černý, D. Mikulová, J. Sís, B. Mašek, H. Jirková, J. Malina, *Proc. Eng.* **2011**, *10*, 3310.

[31] S. C. Baik, S. Kim, Y. S. Jin, O. Kwon, *ISIJ Int.* **2001**, *41*, 290.

[32] O. Khalaj, E. Saebnoori, B. Mašek, C. Štadler, P. Hassas, J. Svoboda, *Metals* **2022**, *12*, 2081.

[33] B. Aminforoughi, S. Degener, J. Richter, A. Liehr, T. Niendorf, *Adv. Eng. Mater.* **2021**, *23*, 2100184.

[34] A. Kromm, S. Brauser, T. Kannengiesser, M. Rethmeier, *J. Strain Anal. Eng. Design* **2011**, *46*, 581.

[35] E04 Committee, *Practice For X-Ray Determination Of Retained Austenite In Steel With Near Random Crystallographic Orientation*, ASTM International, West Conshohocken, PA **2013**.

[36] E. Macherauch, H. Wohlfahrt, *Härterei-Technische Mitteilungen* **1972**, *27*, 230.

[37] A.-C. Dippel, H.-P. Liermann, J. T. Delitz, P. Walter, H. Schulte-Schrepping, O. H. Seeck, H. Franz, *J. Synch. Radiat.* **2015**, *22*, 675.

[38] J. Kieffer, V. Valls, N. Blanc, C. Hennig, *J. Synch. Radiat.* **2020**, *27*, 558.

[39] G. Ashiotis, A. Deschildre, Z. Nawaz, J. P. Wright, D. Karkoulis, F. E. Picca, J. Kieffer, *J. Appl. Crystallogr.* **2015**, *48*, 510.

[40] J. Rodriguez-Carvajal, in *An Introduction To The Program FullProf 2000*, Laboratoire Le´on Brillouin, CEA-CNRS, Saclay, France **2001**.

[41] D. de Knijf, R. Petrov, C. Föjer, L. A. Kestens, *Mater. Sci. Eng. A* **2014**, *615*, 107.

[42] I. de Diego-Calderón, D. de Knijf, M. A. Monclús, J. M. Molina-Aldareguia, I. Sabirov, C. Föjer, R. H. Petrov, *Mater. Sci. Eng. A* **2015**, *630*, 27.

[43] I. de Diego-Calderón, D. de Knijf, J. M. Molina-Aldareguia, I. Sabirov, C. Föjer, R. Petrov, *Rev. Metal* **2015**, *51*, e035.

[44] K. O. Findley, J. Hidalgo, R. M. Huizenga, M. J. Santofimia, *Mater. Des.* **2017**, *117*, 248.

[45] I. S. Yasnikov, A. Vinogradov, Y. Estrin, *Scr. Mater.* **2014**, *76*, 37.

[46] P. Frint, T. Kaiser, T. Mehner, E. Bruder, M. Scholze, B. Mašek, T. Lampke, M. F.-X. Wagner, *Scientific reports* **2019**, *9*, 17023.

[47] X. C. Xiong, B. Chen, M. X. Huang, J. F. Wang, L. Wang, *Scr. Mater.* **2013**, *68*, 321.

[48] J. G. Speer, F. C. R. Assunção, D. K. Matlock, D. V. Edmonds, *Mater. Res.* **2005**, *8*, 417.

[49] R. Ding, A. Zhao D. Tang, *Scr. Mater.* **2014**, *88*, 21.

[50] I. de Diego-Calderón, M. J. Santofimia, J. M. Molina-Aldareguia, M. A. Monclús, I. Sabirov, *Mater. Sci. Eng. A* **2014**, *611*, 201.

[51] E. de Moor, S. Lacroix, A. J. Clarke, J. Penning, J. G. Speer, *Metall. Mater. Trans. A* **2008**, *39*, 2586.

[52] D. V. Edmonds, K. He, F. C. Rizzo, B. C. de Cooman, D. K. Matlock, J. G. Speer, *Mater. Sci. Eng. A* **2006**, *438–440*, 25.

[53] M. J. Santofimia, L. Zhao, R. Petrov, C. Kwakernaak, W. G. Sloof, J. Sietsma, *Acta Mater.* **2011**, *59*, 6059.

[54] G. Masing, in *Wissenschaftliche Veröffentlichungen Aus Dem Siemens-Konzern* (Ed: C.D. Harries), Springer, Berlin, Heidelberg **1923**, pp. 231–239.

[55] G. Masing, *Z. Tech. Phys.* **1925**, *32*, 569.

[56] V. Hauk, in *Structural And Residual Stress Analysis By Nondestructive Methods: Evaluation - Application - Assessment*, Elsevier, Amsterdam **1997**.

[57] E. Jimenez-Melero, N. H. van Dijk, L. Zhao, J. Sietsma, J. P. Wright, S. van der Zwaag, *Mater. Sci. Eng. A* **2011**, *528*, 6407.